Discrete Bubble Modeling of Unsteady Cavitating Flow

Zhiliang Xu,[1,*] Myoungnyoun Kim,[1,*] Tianshi Lu,[1] Wonho Oh,[2,*,**] James Glimm,[1,2,*,**] Roman Samulyak,[1] Xiaolin Li,[2,**] and Constantine Tzanos[3]

[1]*Computational Science Center, Brookhaven National Laboratory,
Upton, NY 11973-5000*
[2]*Department of Applied Mathematics and Statistics, University at Stony Brook,
Stony Brook, NY 11794-3600*
[3]*Reactor Analysis and Engineering, Argonne National Laboratory,
Argonne, IL 60493*

ABSTRACT

A discrete vapor bubble model is developed to simulate unsteady cavitating flows. In this model, the mixed vapor-liquid mixture is modeled as a system of pure phase domains (vapor and liquid) separated by free interfaces. On the phase boundary, a numerical solution for the phase transition is developed for compressible flows. This model is used to study the effect of cavitation bubbles on atomization, i.e., the breakup of a high-speed jet and spray formation. The major conclusion is that a multiscale (three-scale) model is sufficient to achieve agreement with quantitative macroscale flow parameters, such as spray opening angle and spray volume fraction or density, or as a qualitative measure, the occurrence of spray formation. The authors believe this to be the first numerical study of the atomization process at such a level of detail in modeling of the related physics.

NOMENCLATURE

c	sound speed		V	volume
h	bubble spacing		v	vapor
E	specific total energy			
E_C	critical energy		**Greek Symbols**	
E_∞	energy translation			
J	nucleation rate		γ	adiabatic exponent
k_b	Boltzmann's constant		ρ	density
l	liquid		κ	thermal conduction coefficient
M	mass flux		ϵ	specific internal energy
m	mass of a molecule		$\triangle P_C$	critical tension
N	number density of the liquid		σ	surface tension
P	pressure		Σ	Nucleation probability
P_∞	stiffening constant		α	Evaporation coefficient
P_v	vapor pressure		Γ	Gruneisen coefficient
P_C	negative pressure threshold		Δx	Grid spacing
Q_v	heat of evaporization			
R_C	critical radius		**Acronyms**	
Re	Reynolds number			
r	bubble radius		AMR	adaptive mesh refinement
S	specific entropy		CFL	courant, Friedrichs, and Lewy condition
s	speed of the moving phase boundary		EOS	equation of state
T	absolute temperature		MUSCL	monotone upstream-centered schemes for conservation laws
T_s	interface temperature		NS equations	Navier-Stokes equations
t	time			

1. INTRODUCTION

Arisen from high-speed nozzle flows, liquid cavitation, and jet atomization (i.e., jet breakup and spray formation) are great challenges for computational science, as well as for theory. This fact is due to the large range of spatial and temporal scales and the complex flow regimes involved. Fluid mechanisms leading to spray formation are still debated. Fluid surface instabilities, parameters such as nozzle shape, and the internal nozzle flow pattern (such as turbulence and cavitation) all could be possible mechanisms responsible for jet breakup and atomization. For a literature review of jet atomization mechanisms (see [1–3]). Among these mechanisms, unsteady cavitation in fluid flow is a dominant effect in high-speed nozzle flows in many high-pressure injectors. Cavitation bubbles are formed due to the sharp inlet corner of the nozzle and a "vena contracta," i.e., the flow "sticks" to the edges of the opening, thus effectively reducing the size of the opening, inside the nozzle [4]. The simulation of cavitation and the study of its role in the jet atomization is the main goal of the present paper.

Visual observation of cavitation in injectors is difficult because of the small sizes of nozzles [5] and clouds around cavitation bubbles. To further understand cavitation in nozzles, many numerical models have been proposed. Most of them employed a continuum modeling or a single pseudofluid equa-

tion of state for multiphase (bubbly) flows [7]. For this class of methods, the key issue is to develop a proper constitutive law for the mixture [8]. Often the mixture is assumed to be homogeneous and barotropic. Despite its simplicity, this class of methods often lacks an ability to resolve detailed physics, such as drag, surface tension, phase transition, viscous friction between two phases, and other microphysics phenomena. Moreover, cavitation leading to the jet atomization has not been studied for this class of methods. A review of continuum modeling and simulation of cavitating flows in nozzles is given in [9].

In this paper, we follow a different approach in the study of cavitating flows and the jet atomization: the heterogeneous method, or direct numerical simulation. The central part of the proposed method is the discrete vapor bubble model. Our numerical simulation of multiphase systems is based on the front tracking method for explicit numerical resolution of phase boundaries, and the FronTier hydrodynamic code [10–13]. The front tracking method has been used extensively to study fluid interface instability problems, such as fluid mixing, and is capable of resolving complex fluid interfaces. These studies have achieved good agreements with experiments. See also [10–13], and references cited there. The direct numerical simulation is a powerful method for studying multiphase problems based on techniques developed for free surface flows and has already attracted the attention of many researchers.. Welch [14] studied a single vapor bubble in a liquid, including interface tracking with mass transfer while the phase boundary was assumed to exist in thermal and chemical (Gibbs potential) equilibrium. Juric and Tryggvason [15] simulated boiling flows using the incompressible approximation for both liquid and vapor phases, and a nonequilibrium phase transition model with a parameter called kinetic mobility whose value was measured experimentally. In contrast, we solve compressible fluid dynamics equations for both liquid and vapor phases, as the cavitation phenomena depends on nonlinear waves (rarefaction waves) in the liquid. To describe cavitation, a discrete vapor bubble mode, introduced in [6] to describe the mixed phase region, is further developed. Using this model to study cavitation in a Mercury jet has achieved good agreements with experiments [6]. In this model, the liquid-vapor mixture is described by pure phase domains (vapor bubble and liquid) separated by free interfaces. The critical pressure necessary for the formation of a cavitation bubble, the initial radius, and parameters regulating the bubble population are estimated by the homogeneous nucleation theory. The numerical phase boundary solution is obtained by solving the compressible Navier-Stokes equations, which includes the influence of thermal nonequilibrium and the discontinuity of state variables across the phase transition boundary. The only prior information needed to obtain such a phase transition solution is the phase exchange rate coefficient, which is set from experimental considerations. Matsumoto and Takemura [16] studied numerically the influence of internal phenomena on the motion of a single gas bubble with compressible Navier-Stokes equations and the interfacial dynamics of phase transitions. Their governing equation contain more technical details, such as the concentration of noncondensible gas in the liquid and vapor phases. In [16], the temperature field was first solved from the simplified energy equations, and other fields were solved afterward. Our approach updates all fields simultaneously. Therefore, the dynamics of the phase boundary in our approach is coupled to acoustic waves in the interior. Moreover, [16] only studied single bubble dynamics. Multiple bubble dynamics is studied in the present paper.

From a computational point of view, we argue that cavitation and spray formation should be treated as a multiscale phenomena. Macroscopic flow parameters, such as the spray opening angle and the volume fractions of liquid within the spray, are on the scale of centimeter. The finite vapor bubble size, which is essential for the spray formation in our simulations, is on the scale of microns. The dynamics of the moving phase boundary, with mass transfer across the phase boundary, depends on a thermal diffusion layer, having width of the order of nanometers. The model developed in the paper is multiscale and multiphysics. It is applicable to a range of problems involving unsteady cavitating flows. The main conclusion of this paper is that modeling of the mixed phase region in terms of finite-sized vapor bubbles in the liquid achieves macroscopic flow descriptions, such as the spray opening angle and the liquid mass flux within the spray, is in approximate agreement with experimental measurements.

In our study of unsteady cavitating flows leading to spray formation, we neglect some other less important phenomena. For example, turbulence appears not to play a significant role in the nozzle flow. Although the flow Reynolds number is above a critical value for transition, the length of the nozzle is below the critical length and there is not enough time (or distance) for the transition into turbulence. Surface tension is also neglected. It is easy to estimate that the surface tension is not negligible only for submicron-size bubbles for the liquid. Technically, such bubbles are still beyond the current numerical resolution. They occur as nucleation sites and eventually grow into the larger bubbles studied here.

The paper is organized as follows. In Section 2, numerical algorithms implemented in the discrete vapor bubble model are described. To allow the creation of vapor bubbles, a dynamic bubble insertion algorithm is developed and a new type of Riemann problem associated with liquid-vapor phase change is solved. In Section 3.1, the internal nozzle flow is studied. Section 3.2 contains the discrete vapor bubble model simulation results. Section 4 discusses the differences in the predicted results of two models.

2. NUMERICAL ALGORITHMS

Numerical simulations of the jet atomization reported in this paper attempt to accurately reproduce experimental conditions. The schematic of the high-pressure chamber and nozzle are shown in Fig. 1. To simulate the formation of the jet, only inflow boundary conditions with time-dependent pressure are prescribed at the inlet to the chamber. A flow-through boundary condition is used at the flow outlet, and a no slip condition is used at the nozzle wall. The formulation of these boundary conditions follow [22]. Flows in the high-pressure chamber and the formation of the jet are simulated by solving the Navier-Stokes (NS) equations for both the liquid and ambient gas, and the jet–ambient-gas interface is explicitly resolved using the front tracking method. The liquid is treated as viscous and heat conducting. Because the thermal conductivity and the viscosity are both small, the Navier-Stokes equations are solved with an explicit algorithm. In the interior, for the convection terms of the NS equations, a monotone
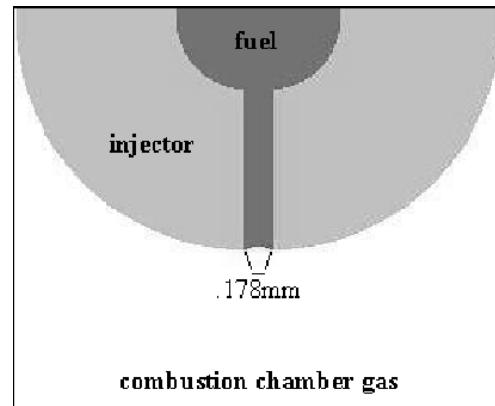

FIGURE 1. Geometry of injection reservoir and nozzle leading to combustion chamber

upstream-centered scheme for conservation laws (MUSCL scheme) [23] is used, which is second order accurate in both space and time, and for the diffusion terms, central differencing is employed. To update a front solution, an operator splitting method is used, which divides into a normal front propagation step and a tangential front propagation step. In the normal front propagation step, a front is propagated to a new position in its normal direction by solving a generalized Riemann problem. The method of characteristics is used to update the states on the two sides of the front at this new position. In the tangential front propagation step, a first-order Lax-Friedrichs scheme is applied.

We adopted the Berger-Colella [24] adaptive mesh refinement (AMR) to the front tracking method by merging *FronTier* with the *Overture* code, the AMR package developed at Lawrence Livermore National Laboratory. All material interfaces are tracked. The tracked interfaces are all covered by the finest level patches. We refer to [25] for additional details. For the simulations presented in this paper, three levels of refinement with a refinement factor 2 were used. The base level has 170×1000 cells on the 1.513 mm $\times$ 8.9 mm domain, which is half of the injection reservoir and combustion chamber as shown in Fig. 1. The finest grid level has a mesh resolution of 2 μm. Therefore, the grid spacing Δx of the finest grid level is $\Delta x = 2$ μm.

The equation of state (EOS) model for the pure liquid phase of the flow is given by a stiffened polytropic equation

$$P + \gamma P_\infty = (\gamma - 1)\rho(\epsilon + E_\infty) \qquad (1)$$

For n-heptane used in the simulations, adiabatic exponent is $\gamma = 3.19$, stiffening constant is $P_\infty = 3000 \text{ bar}$ and energy translation is $E_\infty = 4.85 \times 10^3 \text{ erg/g}$. Here ρ is the density, P is the pressure, and ϵ is the specific internal energy. The thermal conduction of the liquid is $\kappa = 1.3 \times 10^4 \text{ erg/s g K}$. The equation of state for the ambient gas and vapor inside cavitation bubbles used in the simulations is γ-law. The thermal conduction of the n-heptane vapor is $\kappa = 1.3 \times 10^3 \text{ erg/s g K}$.

2.1 Algorithms of the Discrete Vapor Bubble Model

The discrete vapor bubble model is at the technical heart of this paper. We introduce, and resolve, two new length scales in order to achieve experimental agreement for macroscopic descriptions of the flow. The larger of the two new length scales is the vapor bubble radius, resolved at the grid spacing level (microns). The subsequent dynamics of the bubbles depends on a thermal diffusion length scale at the vapor bubble (phase transition) boundary. This layer is measured in nanometeters, and is described here through a subgrid model, as it is below the level of the computational grid.

2.1.1 Critical Bubble Radius

The discrete vapor bubble model accounts for the finite-size effects of the vapor bubbles in the mixed phase flow regime. The mixed phase regime is modeled by vapor bubbles of finite size inserted into the liquid.

Vapor bubbles are formed by liquid vaporization when the liquid pressure P fluctuates and falls below the saturated vapor pressure P_v at given temperature. The pressure fluctuation $\Delta P = P_v - P$, which is a positive quantity if $P_v > P$, is called tension. Physically, a vapor bubble will appear whenever it is thermodynamically favorable. Cavitation is the result of rapid growth of vapor nuclei that be-

come unstable due to a change in ambient pressure. If the maximum size of a nucleus is defined by the radius R_C (critical radius), then at equilibrium, the critical tension $\triangle P_C$ is given by [34,35]

$$\triangle P_C = \frac{2\sigma}{R_C} \qquad (2)$$

where σ is the surface tension of the liquid, and the critical radius of a cavitation bubble is

$$R_C = \frac{2\sigma}{\triangle P_C} \qquad (3)$$

To create such a nucleus with critical radius R_C, a critical energy $E_C = \frac{16\pi\sigma^3}{3\triangle P_C^2}$ [34,35] must be deposited into the liquid to break the barrier against nucleation. This critical energy E_C accounts only for surface energy and the gain in volume energy. The energy needed to convert liquid to vapor (heat of vaporization) is neglected, because it is relatively small. One can write a nucleation rate J

$$J = J_0 \exp^{E_C/(k_b T)} \qquad (4)$$

per unit volume and per unit time. Here, k_b is the Boltzmann's constant, T is the absolute liquid temperature, and J_0 is a factor of proportionality defined as

$$J_0 = N \left(\frac{2\sigma}{\pi m} \right)^{1/2} \qquad (5)$$

where N is the number density of the liquid (molecules/m^3) and m is the mass of a molecule. For N-heptane used in the present study, $m = 1.66 \times 10^{-22}\text{ g}$ and $N = 3.98 \times 10^{27}\text{ molecules}/m^3$. Thus, the nucleation probability Σ in a volume V during a time period t is [36]

$$\Sigma = 1 - \exp^{-J_0 V t \exp^{[-E_C/(k_b T)]}} \qquad (6)$$

Equations (3)–(6) can be used to compute the negative pressure threshold P_C needed to create cavitation bubbles for a given critical radius and nucleation probability. For the nucleation probability $\Sigma = 0.5$, this relation is given by

$$P_C \cong - \left(\frac{16\pi\sigma^3}{3k_bT\ln(J_0Vt/\ln 2)} \right)^{1/2} \qquad (7)$$

We would like to note that Eq. (7) is applicable to only very clean fluids. It is well known that real fluids contain large amount of nucleation centers that increase the cavitation probability, but accurate experimental measurements of critical cavitation parameters are not available. Since we are interested in the simulation of real fluids, we assume that (7) gives the correct functional relation between the critical pressure, volume, and the nucleation probability, whereas the absolute value of the critical volume at a specific value of the critical pressure has to be calibrated through the comparison of simulation results to experimental data. A phenomenological bubble-spacing parameter h is chosen by a series of numerical experiments. By calibrating this parameter, we also account for effects of initial growth of submicron bubbles, as the initial growth stage of these submicron bubbles is not resolved by the current numerical resolution.

2.1.2 Dynamic Creation of Vapor Bubbles

The bubble spacing h, which is defined as the minimum distance between the centers of two newly created bubbles, is controlled at the time of bubble insertion to account for the distribution of nucleation centers and model the effect of microbubble growth-induced pressure reduction on the nucleation probability. For the present study, the default bubble radius at the time of insertion is $r = 2\Delta x = 4\,\mu\mathrm{m}$, which meets the requirement for the minimum numerical resolution. The default bubble spacing is $h = 4r$. The choice of bubble spacing and bubble radius will be discussed in Section 3.1.

The dynamic bubble creation algorithm proceeds as follows. In each cell at every time step, it is checked whether the liquid pressure p is less than -10 bar. Here, -10 bar is the negative pressure threshold P_C estimated using relations given in Section 2.1.1 for the liquid n-heptane used in the present study. The properties of n-heptane is given in Table 1. If there is a $2r \times 2r$ block thats $p < -10$

bar centered in a larger $h \times h$ region, which does not contain bubbles, a circular bubble of radius r is inserted into this block. For the vapor bubble states, the temperature and velocity are set to be the average temperature $\overline{T}$ and velocity $\overline{U}$ of the liquid that occupied this block. From the static Clausius-Clapeyron relation, the initial vapor pressure is set to be $P_{\mathrm{sat}}(\overline{T})$, which is the saturated liquid-vapor pressure at a temperature $\overline{T}$. The vapor density is computed from the EOS.

An application of the discrete vapor bubble model for the description of cavitation in mercury has been presented in [37]. Simulations were performed at conditions typical for the Muon Collider target experiments. Juric and Tryggvason [15] also used the discrete vapor bubble model to simulate film boiling.

2.1.3 Dynamic Phase Boundaries for Compressible Fluids

The phase boundary is modeled as a sharp interface in the present paper. The viscosity and surface tension on the interface are neglected because thermal effects are normally dominant over viscous effects in phase transitions. The phase transition is then governed by the compressible Euler equations with heat diffusion,

$$\rho_t + (\rho u)_x = 0 \qquad (8)$$

$$(\rho u)_t + (\rho u^2)_x + P_x = 0 \qquad (9)$$

$$(\rho E)_t + (\rho E u + Pu - \kappa T_x)_x = 0 \qquad (10)$$

where subscripts t and x are used to denote derivatives with respect to time and space, respectively, $E = 1/2(u^2) + \epsilon$ is the specific total energy, ϵ is the specific internal energy, P is the pressure, κ is the thermal conductivity, and T is the absolute temperature.

Integration of the governing equations across the interface yields the jump conditions for the dynamic phase boundary

TABLE 1. The thermal properties of N-heptane and No. 2 diesel liquid fuel measured at 298 K

Liquid type	Density g/cm^3	Sound speed cm/ms	Dynamic viscosity g/(cm.ms)	Surface tension g/ms^2
N-heptane	0.66	12	0.4×10^{-5}	1.96×10^{-5}
No. 2 diesel	0.843	16.9	0.25×10^{-4}	3×10^{-5}

$$[\rho u] = s[\rho] \tag{11}$$

$$[\rho u^2 + P] = s[\rho u] \tag{12}$$

$$[\rho u E + P u - \kappa T_x] = s[\rho E] \tag{13}$$

where s is the speed of the moving phase boundary and the symbol $[U] = U_{\text{left}} - U_{\text{right}}$ denotes a jump across the phase boundary. Equations (11)–(13) give

$$\rho_{\text{v}}(u_{\text{v}} - s) = \rho_{\text{l}}(u_{\text{l}} - s) \tag{14}$$

$$\rho_{\text{v}}(u_{\text{v}} - s)^2 + P_{\text{v}} = \rho_{\text{l}}(u_{\text{l}} - s)^2 + P_{\text{l}} \tag{15}$$

$$(\rho_{\text{v}} E_{\text{v}} + P_{\text{v}})(u_{\text{v}} - s) - \kappa_{\text{v}} T_{\text{v},x} = (\rho_{\text{l}} E_{\text{l}} + P_{\text{l}})(u_{\text{l}} - s) - \kappa_{\text{l}} T_{\text{l},x} \tag{16}$$

and the change of energy during the phase transition is

$$\epsilon_{\text{v}} + \frac{P_{\text{v}}}{\rho_{\text{v}}} = \epsilon_{\text{l}} + \frac{P_{\text{l}}}{\rho_{\text{l}}} + Q_{\text{v}} \tag{17}$$

where Q_{v} is the heat of vaporization and subscripts l and v denote liquid and vapor, respectively.

For the mass flux $M = \rho_{\text{v}}(u_{\text{v}} - s) = \rho_{\text{l}}(u_{\text{l}} - s)$, the mass and momentum balance equations give

$$M = \frac{u_{\text{v}} - u_{\text{l}}}{\tau_{\text{v}} - \tau_{\text{l}}} \tag{18}$$

$$M^2 = -\frac{P_{\text{v}} - P_{\text{l}}}{\tau_{\text{v}} - \tau_{\text{l}}}, \qquad \tau = \frac{1}{\rho} \tag{19}$$

$$(u_{\text{v}} - s)(u_{\text{l}} - s) = \frac{P_{\text{v}} - P_{\text{l}}}{\rho_{\text{v}} - \rho_{\text{l}}} \tag{20}$$

A combination of these equations with the energy balance equation leads to the generalized Hugoniot relation

$$\epsilon_{\text{l}} - \epsilon_{\text{v}} + \frac{P_{\text{l}} + P_{\text{v}}}{2}(\tau_{\text{l}} - \tau_{\text{v}}) = \frac{1}{M}(\kappa_{\text{v}} T_{\text{v},x} - \kappa_{\text{l}} T_{\text{l},x}) \tag{21}$$

Since the mass flux M is unknown, one more equation is needed to close the system. The kinetic theory of evaporation gives the evaporation rate with a coefficient determined experimentally. Denote the vapor and liquid equilibrium pressure at temperature T by $p_{\text{sat}}(T)$, which satisfies the Clausius-Clapeyron equation. The net mass flux is

$$M_{ev} = \alpha \frac{P_{\text{sat}}(T) - P_{\text{v}}}{\sqrt{2\pi RT}} \tag{22}$$

with given absolute temperature T and pressure p_{v}. Here $R = k_B/m$, where m is the molecular mass and k_B is the Boltzmann constant. α is called the evaporation coefficient or sometimes the condensation coefficient. Research has shown that the value of $\alpha < 1$ results from either impurity of substances or the deficiency in derivation kinetic theory model used to defined α. A formula similar to Eq. (22) was derived by Alty and Mackay [38] for condensation. Reviews of experiments and theories regarding the evaporation coefficient are given in [40,41]. In the present study, a value of 0.4 is used for α. Different values of α have been studied numerically. The conclusion is that influences of α on the phase boundary dynamics is not significant unless it is very small compared to unity [39].

The numerical algorithm for a dynamical phase transition proceeds as follows. The characteristic form of Eqs. (8)–(10) is used at the interface

$$\frac{dP}{d\lambda_+} + \rho c \frac{du}{d\lambda_+} = \Gamma \kappa T_{xx} \tag{23}$$

$$\frac{dP}{d\lambda_-} - \rho c \frac{du}{d\lambda_-} = \Gamma \kappa T_{xx} \tag{24}$$

$$\frac{d\epsilon}{d\lambda_0} + p\frac{d\tau}{d\lambda_0} = \frac{1}{\rho}T_{xx} \tag{25}$$

where $c = \sqrt{(\partial P/\partial \rho)_S}$ is the sound speed, S is the specific entropy, and Γ is the Gruneisen coefficient. The characteristic derivatives λ_+, λ_-, and λ_0 are defined by

$$\frac{d}{d\lambda_+} = \frac{\partial}{\partial t} + (u+c)\frac{\partial}{\partial x}$$
$$\frac{d}{d\lambda_-} = \frac{\partial}{\partial t} + (u-c)\frac{\partial}{\partial x}$$
$$\frac{d}{d\lambda_0} = \frac{\partial}{\partial t} + u\frac{\partial}{\partial x}$$

The phase boundary conditions are (18)–(21) and (22). To determine the interface temperature, it is postulated that the temperatures of liquid and vapor at the interface are continuous $T_s = T_l = T_v$. This approach was also used in [44]. Thus, the interface temperature T_s is coupled to the phase transition equations.

To solve the characteristic system with the phase boundary conditions, an iteration algorithm is developed. Backward characteristics are traced from an estimated location of the phase boundary at the next time step. States at the feet of these characteristics (at the current time level) are first obtained by interpolation. The characteristic speeds are $\lambda_\pm = u \pm c$ and $\lambda_0 = u$, whereas the phase transition

interface moves at a speed $s = \Delta(\rho u)/\Delta\rho$. For a small time step Δt, the characteristics are approximated by straight lines. Figure 2 is a schematic diagram showing the backward characteristics. The left foot is $(c_l + u_l - s)\Delta t$ away from the interface, while the right foot is $(c_r - u_r + s)\Delta t$ away from the interface. During the iteration, the characteristics are obtained by explicit formulas, and are thus obtained once only per time step, external to the thermodynamic iteration. This simplification of characteristics is valid because $s \ll c$. Once the states at the characteristic feet are obtained by interpolation, the characteristic equations are solved by integrating along the characteristics.

Assuming that the vapor is on the right side, the algorithm can be described as follows:

1. Substituting the vapor pressure at S_{0+} for P_v in Eq. (22) and discretizing (21), we have two equations that we solve for the two unknown variables T_s and M. The function P_{sat} is a nonlinear function. Since this step itself is in the iteration of P_v and $\Delta\tau$, the Clausius-Clapeyron equation is linearized at a reference temperature T_v and solved for T_s and M while preserving the convergence of S_l^* and S_r^* in Fig. 2 through the iteration. For the first iteration step, T_v can be chosen to be equal to T_s at the beginning of the time step if $T_{0-} = T_{0+}$. For subsequent iteration steps, T_v is simply the T_s obtained in the last iteration. On linearization, we obtain solutions
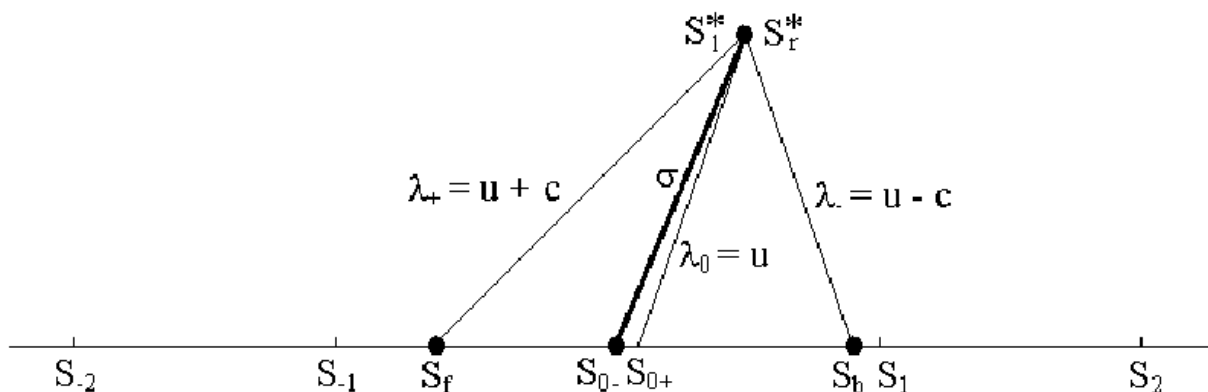

FIGURE 2. Stencil for the phase boundary propagation. The new front states S_l^* and S_r^* are calculated

$$T_s = \frac{\kappa_\mathrm{l} T_{-1} + \kappa_\mathrm{v} T_1 + \frac{\alpha}{\sqrt{2\pi R T_v}} \left[Q_\mathrm{v} - \bar{\tau}(P_\mathrm{v} - P_\mathrm{l})\right] \Delta x \left[P_\mathrm{v} - P_\mathrm{sat}(T_\mathrm{v}) + \frac{\mathrm{d}p_\mathrm{sat}}{\mathrm{d}T}(T_\mathrm{v}) T_\mathrm{v}\right]}{\kappa_\mathrm{l} + \kappa_\mathrm{v} + \frac{\alpha}{\sqrt{2\pi R T_\mathrm{v}}} \left[Q_\mathrm{v} - \bar{\tau}(P_\mathrm{v} - P_\mathrm{l})\right] \Delta x \frac{\mathrm{d}P_\mathrm{sat}}{\mathrm{d}T}(T_\mathrm{v})} \tag{26}$$

and

$$M_{ev} = \frac{\alpha}{\sqrt{2\pi R T_\mathrm{v}}}$$
$$\times \left[P_\mathrm{sat}(T_\mathrm{v}) - P_\mathrm{v} + \frac{\mathrm{d}P_\mathrm{sat}}{\mathrm{d}T}(T_\mathrm{v})(T_s - T_\mathrm{v})\right] \tag{27}$$

where $\frac{\mathrm{d}P_\mathrm{sat}}{\mathrm{d}T}(T_\mathrm{v})$ is the slope of phase coexistence curve at T_v by Clausius-Clapeyron equation. Here, $\bar{\tau}$ is $\bar{\tau} = \frac{\tau_\mathrm{v} + \tau_\mathrm{l}}{2}$.

2. Having obtained the temperature T_s and mass flux M_{ev}, the characteristic equations (23) and (24) are solved with the Rankine-Hugoniot conditions (18) and (19). For the first iteration, the $\Delta\tau$ in (18) and (19) is set to $\tau_{v0} - \tau_{l0}$. The location of the backward characteristic during the iteration steps is not changed because $s \ll c$. The density ρ_l^* and ρ_v^* are determined from their EOS's with the pressure and temperature obtained in the iteration.

3. Convergence of the iteration is controlled by P_v and $\Delta\tau$. The last step in the iteration is to compare the newly obtained p_v and $\Delta\tau$ to the values from the previous the iteration. The relative error is defined to be the difference between a value from the current iteration step and that from the previous iteration divided by the value from the current iteration. If the relative errors of both P_v and $\Delta\tau$ are smaller than the given tolerances, the iteration is over. Otherwise, we update the P_v and $\Delta\tau$ for next iteration and go back to step 1. In the present study, the tolerances for P_v and $\Delta\tau$ have the value 10^{-9}.

The phase transition problem depends on a subgrid model to describe the thermal layer at the phase transition boundary. Because the width of the thermal layer of the liquid is proportional to $\sqrt{\kappa t/\rho c_\mathrm{p}}$, and the time step is restricted by the Courant, Friedrichs, and Lewy (CFL) condition $dt = dx/c$,

which states that the domain of dependence of hyperbolic PDEs must lie within the domain of dependence of the finite difference scheme at each mesh point to guarantee the stability of an explicit finite difference scheme, it usually requires $10^3 \sim 10^4$ steps for the liquid thermal layer to expand to a micron-scale grid cell. If the thermal layer is thinner than a grid cell in the finite difference scheme, the temperature profile takes the form

$$T \approx T_\mathrm{p} + (T_{-1} - T_\mathrm{p}) \left(\frac{x}{\sqrt{4\nu t}}\right) \tag{28}$$

where T_p is the phase boundary temperature, T_{-1} is the temperature one grid cell away from the phase boundary, and $\nu = \frac{\kappa t}{\rho c_\mathrm{p}}$. Thus the temperature gradient at the interface is approximated by

$$\frac{\partial T}{\partial x} \approx \frac{T_{-1} - T_\mathrm{p}}{\sqrt{\pi \nu t}} \tag{29}$$

The interfacial heat flux in the form of $\frac{\kappa \Delta T}{\Delta x}$ should be replaced by the above approximation. When the thermal layer is wider than a grid cell, the conventional finite difference approximation of the temperature gradient at the interface gives satisfactory results.

This is a new description of the Riemann problem associated with a phase transition in a fully compressible fluid. Mass transfer across an interface due to the phase change is allowed. Thus, the interface motion also depends on the phase change under nonequilibrium thermodynamic and hydrodynamic conditions. The details of the numerical study of phase boundaries are reported in [39].

3. SIMULATION RESULTS

For studies presented in this paper, fluid and jet nozzle parameters have been chosen to be in the atomization regime, which is typical of diesel jet fluid injection, following experiments performed at Argonne National Laboratory [17] (see Fig. 1). The

nozzle diameter is 0.178 mm, and its length is 1 mm. A finite pulse of diesel fuel is injected into a chamber of SF_6 (a heavy, inert gas chosen to emulate the density of compressed air in a diesel engine). In 0.3 ms, the pressure of injected fuel rises linearly from 1 to 500 bar, then it is maintained at this level for 0.4 ms, and subsequently, it drops linearly to 1 bar over 0.1 ms. Synchrotron x-ray imaging of fuel flow parameters, such as the spray opening angle, the mass distribution of fuel, and the jet tip velocity evolution [17–20], provide important information for the validation of numerical experiments. In this paper, n-heptane is used for calculations as a substitute for diesel fuel used in [17–20] because data for the thermodynamic properties, such as the vapor-liquid saturation, were not available for diesel fuel. The thermodynamic properties of n-heptane, the major component of this fuel, are described in [21]. In Sec. 2.1.3, the vapor-liquid saturation is critical in formulating a numerical solution for interfacial phase change. The thermal and mechanical properties of these two fuels are compared in Table 1.

3.1 Flow in the Nozzle

In this section, we present numerical simulation results of a flow in the nozzle. We first identify that cavitation is an important process. Then, we obtain an estimate on initial bubble radius and bubble spacing. Because of the symmetry, only 1/2 of the nozzle was simulated, which has a 0.088 mm × 1.0 mm domain. We thus afford simulations on a finer grid. This domain is discretized into 80 × 910 cells, with $\Delta x = 1\,\mu$m. A constant pressure flow-through boundary condition is used at the nozzle exit. The exit pressure is set to be 1 bar.

In the first simulation, the flow in the nozzle was assumed to be pure liquid (the bubble insertion algorithm was turned off). With a liquid density 0.66 g/cm^3, mean velocity 100 m/s, and dynamic viscosity 0.004 g/(cm s), the Reynolds number $\mathrm{Re} = 3.3 \times 10^4$ greatly exceeds the critical value for transition to turbulence. Strong vorticity was observed only near the nozzle boundary layer, which was essentially laminar in nature (see Fig. 3). However, the development of boundary layer separation or turbulence was not observed. The distance from the pipe entrance to the location where the transition to turbulent flow is first fully developed con-
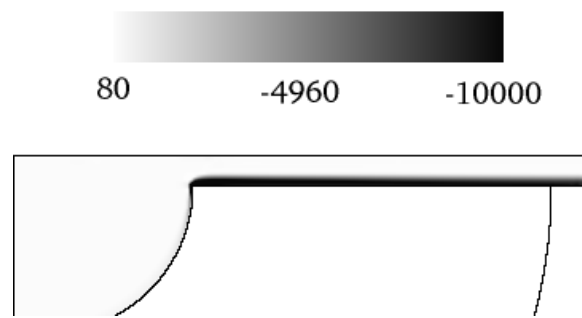

FIGURE 3. Vorticity in the nozzle

stitutes the theoretical initial length of the laminar flow and its magnitude is, approximately,

$$l = 0.03d \times \mathrm{Re} \qquad (30)$$

where d is the pipe diameter [26]. For $\mathrm{Re} \cong 10^4$, it is about 300 pipe diameters. On the experimental side, according to the measurements performed by Kirsten [27] and by Szablewski [28], it ranges from 25 to 100 pipe diameters. Because the length of the nozzle simulated here is five pipe diameters, transition to fully turbulent flow is not expected.

The simulation showed regions with large values of "negative pressure" (Fig. 4), which indicated
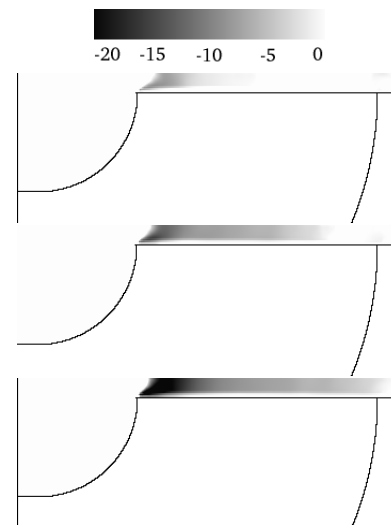

FIGURE 4. The pressure field of the flow at consecutive times. (The unit of pressure is bar. Pressure above 0 bars is represented as white color)

the likely regions of cavitation. Figure 4 shows snap shots of pressure field at consecutive times, from the top frame to the bottom, t = 2.54×10^{-5} s, 2.66×10^{-5} s, and 2.92×10^{-5} s. The negative pressure first appears at the upstream corner. Increasing inlet pressure causes the negative pressure to extend throughout the nozzle.

To simulate cavitation, the discrete vapor bubble approach to cavitation was then used. Usually, cavitation parameters, such as the nuclei density for the bubble growth, need to be determined through experiments. For the present problem we study, these data are not available. We have performed a series of numerical simulations with various values of the bubble spacing parameter and critical bubble radius. Figure 5 includes snapshots of flow interface plots that show simulations with different critical bubble radii, respectively, at 3×10^{-5} s. This set of simulations displays similar bubble distribution, and void fraction values are approximately the same. Here, the void fraction is defined as the ratio of the vapor volume to the volume of the nozzle. We conclude that the critical bubble radius is not a sensitive parameter. Figure 6 shows snapshots of flow interface plots with varied bubble spacing parameter h and a fixed critical bubble radius $r = 2\,\mu$m at 3×10^{-5} s. The simulations of flow in the nozzle exhibited some sensitivity to the bubble spacing parameter in terms of the void fraction of the flow inside the nozzle. The bubbles display similar distribution. However, the void fraction varies in these simulations. The void fraction is larger for smaller
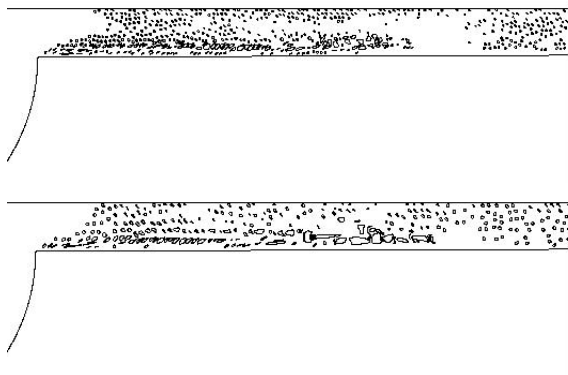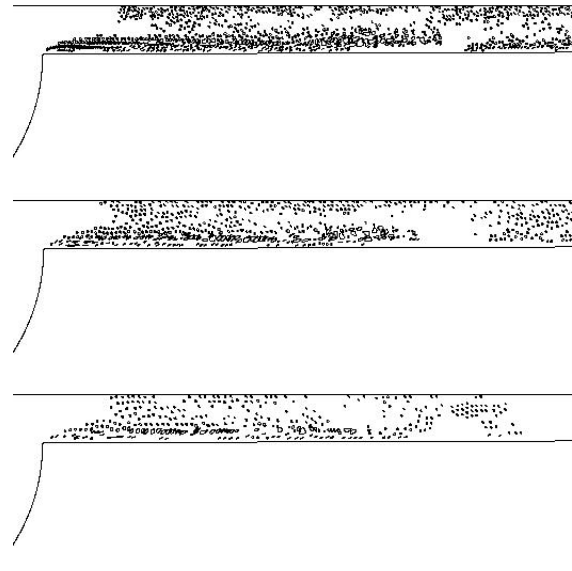

FIGURE 6. The flow interface plots with different bubble spacing. $r = 2\,\mu$m in these simulations. Above: $h = 3r$. Middle: $h = 4r$. Below: $h = 5r$

bubble spacing. Although we are not able to study the dependence of the parameters on the grid for the jet atomization due to the limits of the computational resources, the numerical convergence for the nozzle flow is studied. In this study, the fixed values of critical bubble radii and the bubble spacing parameter are used. We set $r = 4\,\mu$m, and $h = 4r$. Figure 7 shows the flow interface plots on a mesh

FIGURE 5. The flow interface plots with different critical bubble radius. Above: $r = 2\,\mu$m. Below: $r = 3\,\mu$m
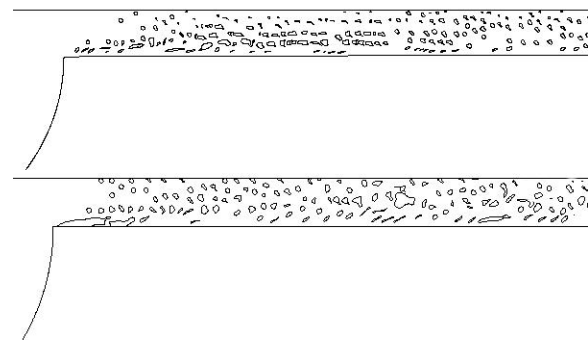

FIGURE 7. The flow interface plots with bubble radius $r = 4$ microns on different meshes. $h = 4r$. Above: grid spacing $\Delta x = 1$ micron. Below: grid spacing $\Delta x = 2$ microns

with the grid spacing $\Delta x = 1\,\mu\mathrm{m}$ and a mesh with the grid spacing $\Delta x = 2\,\mu\mathrm{m}$, respectively. They display similar bubble distribution and void fraction. Based on this study, we conclude that the mesh with the grid spacing $\Delta x = 2\,\mu\mathrm{m}$ is sufficient to resolve the dynamics of this bubbly flow. The solution is convergent in the sense of the predictions of the similar bubble distribution and the void fraction. The mesh with the grid spacing $\Delta x = 2\,\mu\mathrm{m}$ is feasible for the study of jet atomization from the computational point of view. On the other hand, jet atomization, which is the breakup of the downstream flow, was always predicted for various spac-

ing parameters (see Fig. 8). Simulations with different h values exhibited quantitatively similar behavior on the average and were all within the scope of the experimental regime. More details of simulations of jet atomization will be given in Sec. 3.2. Similar studies were performed in [6] for the case of cavitation of mercury under large external energies (the interaction with an intense proton pulse). Because of the large external energies, the results of [6] were insensitive to the bubble spacing and initial radius, and the presence of cavitation was itself sufficient for obtaining the correct evolution of the flow.
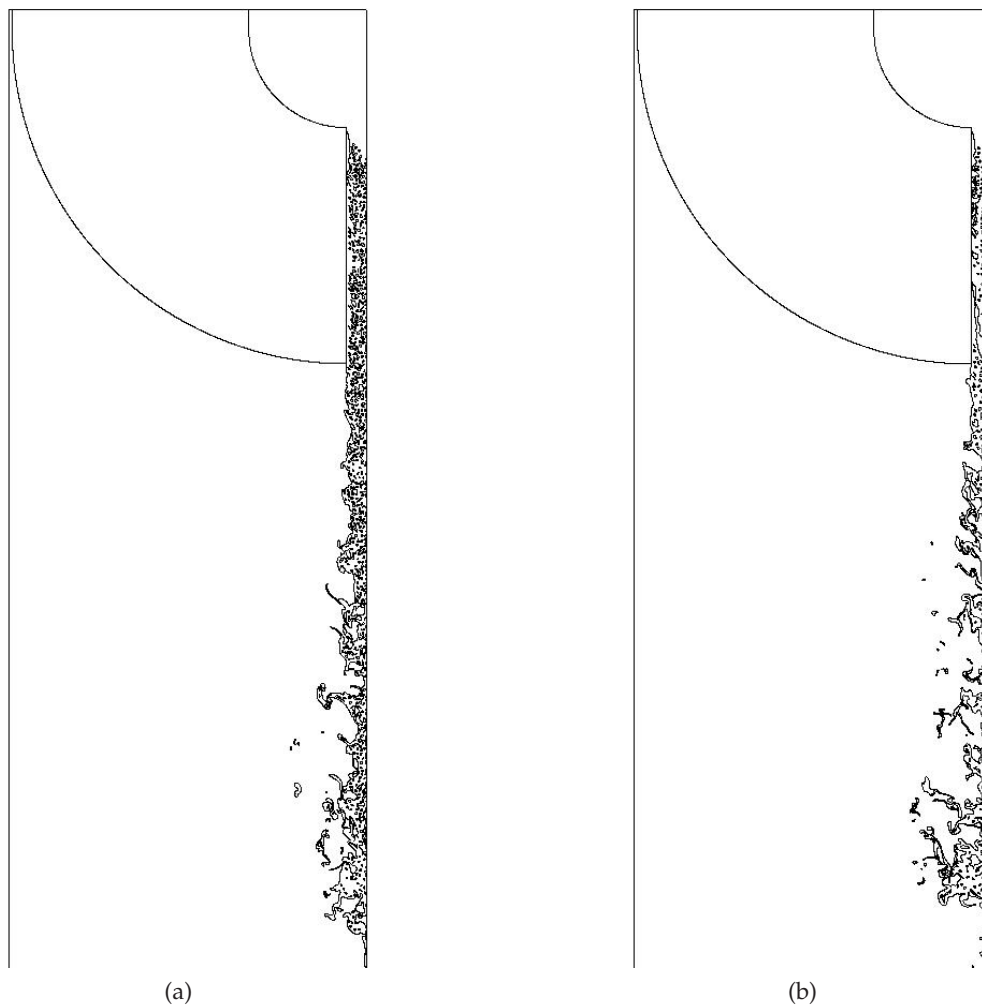

(a)　　　　　　　　　　　　　　(b)

FIGURE 8. Plot of jet interface at late time. **(a)** is bubble spacing = $3r$. **(b)** is bubble spacing = $4r$

3.2 Jet Atomization

The algorithms described in Sec. 2 were used to simulate cavitation, jet breakup, and spray formation. In the simulations, vapor bubbles were created inside the nozzle. These bubbles then were carried downstream outside the nozzle by the flow, and new bubbles continued to form in the nozzle. The disturbance of the cavitation bubbles produced upstream significantly impact the downstream jet breakup. These vapor bubbles grew and broke the jet surface, forming spray, and droplets. We did simulations using two different bubble spacing parameter, namely, $h = 3r$ and $h = 4r$, respectively. We found both simulation results agreed with the experiment. Figure 8 shows the snapshot of the spray development simulated using different spacing parameters. Figures 8(a) and 8(b) display similar small opening angles for the bubble spacing parameter $h = 3r$ and $h = 4r$, respectively. Both are within the experimental range [20] (see also Fig. 2 in [20]).

The simulation predictions were compared to experimentally measured quantities [17–20], such as the fuel mass along the central axis of the spray and the tip velocity of the jet. These experiments measured mass vs. time in a 0.55 mm wide observation window, which is centered 1 mm from the nozzle exit. Aswith the experiments, the simulations also predicted a peak mass. But the width of the peak is less than that of the experimentally measured peak. After the peak, the mass predicted by the discrete vapor bubble model exhibits some oscillations near experimental values (see Fig. 9).
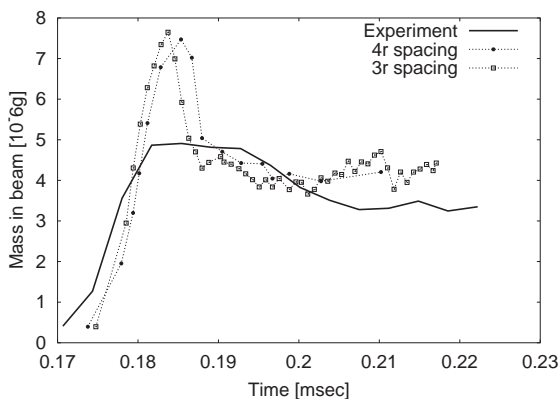
Figure 10 shows the simulated jet tip velocities compared to experimental data. Both simulations agreed with the experimental value on average. The simulation with $h = 4r$ exhibited oscillations, whereas the simulation with $h = 3r$ is quite smooth. It should be noted that the experimental data have been averaged over 100 injection cycles to remove fluctuations.

To test the importance of compressibility and structure of the multiphase mixture in the jet, we performed simulations using the gamma law gas EOS model (easily compressible) for the liquid as well as the stiffened EOS model (practically incompressible) that describes a single phase liquid. Figures 11(a) and 11(b) are front plots of the jet produced from simulations using the gamma law EOS model and the stiffened EOS model, respectively. From these two figures, we see that the jet simulation using the gamma law EOS exhibited expansion, whereas the jet obtained from the simulation using the stiffened EOS model did not exhibit expansion. This comparison shows the dependence of the simulation prediction of the opening angle of the jet on the EOS model. The bubbly flow mixed phase EOS is intermediate between the gamma law gas EOS, and the stiffened gamma law gas EOS, i.e., the bubbly liquid, is intermediate between the gas and the liquid. We conclude that the compressibility of the bubbly liquid in the jet is critical for obtaining the correct opening angle of the jet. In the discrete vapor bubble model, this compressibility is achieved through the expansion of discrete bubbles. The heterogeneous structure of the multiphase flow is nec-
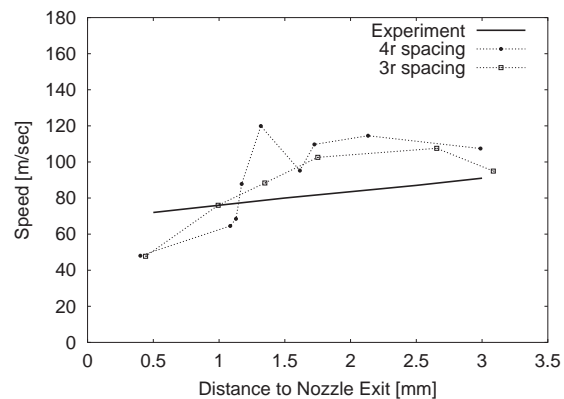

FIGURE 9. Plot of mass through a narrow window located 1 mm from the nozzle exit

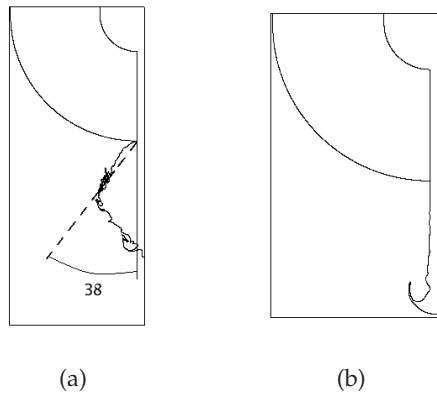**FIGURE 10.** Plot of jet tip velocity

(a)   (b)

FIGURE 11. (a) The front plot of the jet from the gamma law EOS model. **(b)** The front plot of the jet from the stiffened EOS model

essary for obtaining the jet breakup and atomization.

4. CONCLUSIONS

A discrete vapor bubble model to describe multiphase (cavitating) flows was developed. In the discrete vapor bubble model, the vapor-liquid mixture is modeled as two pure phase domains describing vapor bubbles of finite size inserted into the liquid and separated from the liquid by interfaces. A dynamic bubble creation algorithm was formulated to allow vapor bubble insertion, and a new description of the Riemann problem associated with a phase transition was developed. The phase transition Riemann problem depends on a subgrid model to describe the thermal layer at the phase transition boundary.

The discrete vapor bubble model was applied to the direct numerical simulations of cavitating flows. The simulations show jet breakup and atomization in agreement with experiments.

The discrete vapor bubble model predicted cavitating regions made of many microbubbles that led to jet breakup. It displays the influence of the disturbances brought by the finite-size cavitation bubbles that causes atomization. The authors believe this to be the first direct numerical simulation of the impact of cavitation bubbles on atomization. The results indicate that the importance of resolving at a detailed level of multiscale science the physics of unsteady

cavitating flows. The discrete vapor bubble model developed in the present paper contains free parameters, such as critical bubble radii and bubble spacing. The choice of parameters for the discrete vapor bubble model must be carefully examined with respect to different applications. Finally, this work was mainly focused on the simulation of the two-phase mixture resulting from cavitation. The influence of other parameters on spray formation is a subject of further research.

REFERENCES

1. Reitz, R. D., and Bracco, F. V., Mechanism of atomization of a liquid jet, *Phys. Fluids*. **25**:1730–1742, 1982.

2. Reitz, R. D., and Bracco, F. V., *Mechanisms of breakup of round liquid jets*, *The Encyclopedia of Fluid Mechanics*. Gulf Pub. lishing, Houston, Texas, 1986.

3. Lin, S. P., and Reitz, R. D., Drop and spray formation from a liquid jet, *Annu. Rev. Fluid Mech.* **30**:85–105, 1998.

4. Bergwerk, W., Flow pattern in diesel nozzle spray holes, *Proc. Inst. Mech. Eng.* **173**(25):655–660, 1959.

5. Chaves, H., Knapp, M., Kubitzek, A., and Obermeier, F., Experimental study of cavitation in the nozzle hole of diesel injectors using transparent nozzles. *SAE Paper* No. 950290:199–211, 1995.

6. Samulyak, R., Lu, T., Prykarpatskyy, Y., Glimm, J., Xu, Z., and Kim, M. N., Comparison of heterogeneous and homogeneous numerical approaches to cavitation modeling, *Int. J. Multiscale Comp. Eng.* (in press).

7. Schmidt, D. P., Rutland, C. J., Corradini, M. L., Roosen, P., and Genge, O., Cavitation in two-dimensional asymmetric nozzles, SAE International Congress, *SAE Paper* No. 1999-01-0518, 1999.

8. Ventikos, Y., and Tzabiras, G., A numerical method for the simulation of steady and unsteady cavitating flows, *Comput. Fluids*. **29**:63–88, 2000.

9. Schmidt, D. P., and Rutland, C. J., and Corradini, M. L., A fully compressible, two-dimensional, model of small, high speed, cav-

itating nozzles, *Atomization Spray*. **9**(3):255–276, 1999.

10. Bukiet, B., Gardner, C. L., Glimm, J., Grove, J. W., Jones, J., McBryan, O., Menikoff, R., and Sharp, D. H., Applications of front tracking to combustion, surface instabilities and two-dimensional Riemann problems. In *Transactions of the Third Army Conference on Applied Mathematics and Computing, ARO Report No. 86–1*, 223–243, 1986.

11. Glimm, J., Graham, M. J., Grove, J. W., Li, X.-L., Smith, T. M., Tan, D., Tangerman, F., and Zhang, Q., Front tracking in two and three dimensions, *Comput. Math. Appl.* **35**(7):1–11, 1998.

12. Glimm, J., Grove, J. W., Li, X.-L., Shyue, K.-M., Zhang, Q., and Zeng, Y., Three dimensional front tracking, *SIAM J. Sci. Comp.* **19**:703–727, 1998.

13. Glimm, J., Grove, J. W., Li, X.-L., and Tan, D. C., Robust computational algorithms for dynamic interface tracking in three dimensions, *SIAM J. Sci. Comput.* **21**:2240–2256, 2000.

14. Welch, W. J., Local simulation of two-phase flows including interface tracking with mass transfer, *J. Comp. Phys.* **12**:142–154, 1995.

15. Juric, D., and Tryggvason, G., Computations of boiling flows, *Int. J. Multiphase Flow.* **24**(3):387–410, 1998.

16. Matsumoto, Y., and Takemura, F., Influence of internal phenomena on gas bubble motion, *JSME Int. J.* **B37**:288–296,1994.

17. MacPhee, A. G., Tate, M. W., and Powell, C. F., Yue, Y., Renzi, M. J., Ercan, A., Narayanan, S., Fontes, E., Walther, J., Schaller, J., Gruner, S. M., and Wang, J., X-ray imaging of shock waves generated by high pressure fuel sprays, *Science*. **295**:1261–1263, 2002.

18. Powell, C. F., Yue, Y., Gupta, S., McPherson, A., Poola, R., and Wang, J., Development of a quantitative measurement of a diesel spray core using synchrotron X-rays, *Eighth International Conference on Liquid Atomization and Spray Systems, Pasadena, CA*, 2000.

19. Powell, C. F., Yue, Y., Poola, R., and Wang, J., Time resolved measurements of supersonic fuel sprays using synchrotron x-rays, *J. Synchrotron Rad.* **7**:356–360, 2000.

20. Powell, C. F., Yue, Y., Poola, R., Wang, J., Lai, M., and Schaller, J., Quantitative X-ray measurements of a diesel spray core. In *Proc. 14th Annual Conference on Liquid Atomization and Spray Systems (ILASS), Dearborn, MI*, 2001.

21. Starling, K. E., *Fluid Thermodynamic Properties for Light Petroleum Systems*, Gulf Pub. lishing, Houston, 1973.

22. Poinsot, T. J., and Lele, S. K., Boundary conditions for direct simulations of compressible viscous flows, *J. Comput. Phys.* **101**:104–129, 1992.

23. Colella, P., A direct Eulerian MUSCL scheme for gas dynamics, *SIAM J. Comput.* **6**(1):104–117, 1985.

24. Berger, M., and Colella, P., Local adaptive mesh refinement for shock hydrodynamics, *J. Comput. Phys.* **82**:64–84, 1989.

25. Glimm, J., Li, X.-L., and Xu, Z.-L., Front tracking algorithm using adaptively refined meshes. In *Proceedings of Chicago Workshop on Adaptive Mesh Refinement Theory and Applications, Sept. 3-5, 2003*, Springer, Lecture Notes in Computational Science and Engineering, Vol. 41, Plea, Tomasz; Lined, Timor; Weirs, V., Gregory (eds.), 2005.

26. Schlichting, H., *Boundary Layer Theory*, Mcgraw-Hill, New York, 1960.

27. Kirsten, H., Experimentelle Untersuchungen der Entwicklung der Geschwindigkeitsverteilung der turbulenten Rohrstromung, Ph.D. thesis, Leipzig, 1927.

28. Szablewski, W., Der einlauf einer tubulenten rohrstromung, *Ing. Arch*. **21**:323–330, 1953.

29. Wallis, G., *One-Dimensional Two-Phase Flow*, McGraw-Hill, New York, 1969.

30. Samulyak, R., and Prykarpatskyy, Y., Richtmyer-Meshkov instability in liquid metal flows: Influence of cavitation and magnetic fields, *Math. Comput. Simul.* **65**:431–446, 2004.

31. Glimm, J., Li, X. L., Oh, W., Marchese, A., Kim, M.-N., Samulyak, R., and Tzanos, C., Jet breakup and spray formation in a diesel engine. In *Proceedings of 2nd MIT Conference on Computational Fluid and Solid Mechanics*. Cambridge,

MA, SUNY Stony Brook Preprint No. susb-ams-02-20, 2003.

32. Miles, J. W., On the disturbed motion of a plane vortex sheet. *J. Fluid Mech.* **4**:538–552, 1958.

33. Foglizzo, T., and Ruffert, M., An analytic study of bondi-hoyle-lyttleton accretion, *Astron. Astrophys.* **347**:901–914, 1999.

34. Brennen, C. E., *Cavitation and Bubble Dynamics*, Oxford University Press, New York, 1995.

35. Landau, L., and Lifshitz, E., *Statistical Physics*, Pregamon Press, Oxford, 1980.

36. Balibar, S., and Caupin, F., Metastable liquids, *J. Phys. Condensed Matter*. **15**:s75–s82, 2003.

37. Samulyak, R., Lu, T., Prykarpatskyy, Y., Glimm, J., Xu, Z., and Kim, M. N., Comparison of direct and homogeneous numerical approaches to cavitation modeling, *Accepted Int. J. Multiscale Comput. Eng.* **4**:377–389, 2006.

38. Alty, T., and Mackay, C. A., The accommodation coefficient and the evaporation coefficient of water, *Proc. R. Soc. London*, Ser. A, **149**:104–116, 1935.

39. Lu, T., and Xu, Z. L., and Samulyak, R., and Glimm, J., and Ji, X. M., Dynamic Phase Boundaries for Compressible Fluids Siam J. on Scientific Computing, Submitted. Stony Brook preprint No. sunysb-ams-06-07, 2006. (in print)

40. Hagen, D. E., Schmitt, J., Trueblood, M., and Carstens, J., White, D. R., and Alofs, D. J., Condensation coefficient measurement for water in the umr cloud simulation chamber, *J. Atmos. Sci.* **46**:803–816, 1989.

41. Carey, V. P., *Liquid-Vapor Phase-Change Phenomena*. Hemisphere Publishing Corporation, New York, NY, 1992.

42. Caginalp, G., and Socolovsky, E. A., Computation of Sharp Phase Boundaries by Spreading: The Planar and Spherically Symmetric Cases, *J. Comput. Phys.* **95**:85–100, 1991.

43. Kim, Y.-T., Provatas, N., Goldenfeld, N., and Dantzig, J., Universal dynamics of phase-field models for dendritic growth, *Phys. Review E.* **59**(3):R2546–R2549, 1999.

44. Huang, A., and Joseph, D. D., Instability of the equilibrium of a liquid below its vapor between horizontal heated plates, *J. Fluid Mech.* **242**:235–247, 1992.